Modeling Planar Arbitrarily Shaped Microstrip Elements in Multilayered Media

Ming-Ju Tsai, Franco De Flaviis, Owen Fordham, and Nicolaos G. Alexopoulos, *Fellow, IEEE*

***Abstract*—Microstrip elements of arbitrary shape are modeled in multilayered media. The Green's function for the multilayered structure is developed in a form useful for efficient computation for interacting microstrip elements, which may be located at any substrate layer and separated by an arbitrarily large distance. This result is of significant value to a variety of applications in wave propagation besides those discussed in this paper. The mixed-potential integral-equation (MPIE) method is developed in the spatial domain. Examples for regularly/arbitrarily shaped geometries in single and multilayered media are presented. These involve the optimization of an open-end microstrip, a radial-stub microstrip, a five-section overlay-gap-coupled filter, and a circular-patch proximity-coupled microstrip antenna. Very good agreement with measurement and other published data is observed.**

I. Introduction

In THE DESIGN of microwave monolithic integrated circuits (MMIC's) and millimeter-wave integrated circuits, electromagnetic (EM) modeling of microstrip elements (interconnects, antennas, and circuits) becomes important as the operating frequency becomes higher. Full-wave analysis includes the effects of EM coupling, surface waves, and radiation loss while traditional quasi-static methods [1], [2] and equivalent waveguide models [3] fail to yield sufficiently accurate results. Moreover, the ability to analyze circuits of arbitrary shape embedded in a multilayered medium allows for more versatile designs with higher density. The authors have selected the mixed-potential integral equation (MPIE) method [4]–[7] combined with triangular-patch function [8] to solve this general configuration. The MPIE applied in the spatial domain was determined to be more efficient for numerical modeling of arbitrarily shaped printed circuits than the electric-field integral equation (EFIE) techniques applied in the spectral domain [9]. In addition, this method gives a better physical interpretation of current flow and field distribution. The triangular basis function has been successfully used to solve irregular scatterers [8], [10], and [33]. It describes the vector surface current, matches the boundary conditions with no normal components along the boundary edges, and has the potential to represent nonplanar current flow. The unknown current distribution on microstrip elements can be modeled very accurately with triangular basis functions used in the method of moments (MoM's).

Derivation of the spatial-domain dyadic Green's function begins with closed-form formulation in the spectral domain. Several papers using the MPIE formulation have given explicit expressions for single-layered or double-layered structures [12]–[15]. The field and source points were assumed to be embedded in the same layer, which is not applicable for cases with more than three layers. In this paper, the authors derive two different formulations for multilayered structures, and the position of the field point dictates which formulation is chosen. This Green's function can be evaluated without difficulty for any number of layers. To obtain the Green's function in the spatial domain, Sommerfeld integrals must be evaluated. Recently, the complex image method (CIM) [14], [15] was proposed to approximate the integrand with several complex exponential terms, making the computation very efficient. However, the following parameters must be determined before applying the CIM: sampling range, expansion terms, and surface-wave poles. The first two parameters depend strongly on the properties of the layers, and the surface-wave poles of a medium with more than three layers are difficult to find. Therefore, the CIM is not well suited for general geometries with multiple layers. Instead, the authors employ the traditional quadrature method to evaluate Sommerfeld integrals, and apply several techniques to speed up the computations.

The MPIE–MoM analysis presented here starts by meshing the whole geometry with small triangular facets using the meshing algorithm developed by [16]. The spatial-domain Green's function is evaluated over the range of microstrip elements using Sommerfeld integrals, then stored as numerical tables for interpolation. Galerkin's procedure is followed to create a matrix equation from the MPIE. These procedures will be discussed in Section II. Four examples have been investigated and compared with either measurements or published data in Section III.

II. MPIE Formulation

A generalized multilayered medium is shown in Fig. 1. Each substrate layer i has a thickness d_i, and relative permit-

Manuscript received June 16, 1995; revised October 21, 1996. This work was supported by a U.S. Army Research under Grant DAAH 04-93-G-0228, by Hughes-UC Microelectronics under Contract 94-005, and TRW-UC Microelectronics under Contract GA3779RA3S.

M.-J. Tsai was with Electrical Engineering Department, University of California at Los Angeles (UCLA), Los Angeles, CA 90095 USA. He is now with Bell Laboratories, Lucent Technologies, Murray Hill, NJ 07974-0636 USA.

F. De Flaviis and O. Fordham are with the Electrical Engineering Department, California State University at Los Angeles (UCLA), Los Angeles, CA 90095 USA.

N. G. Alexopoulos was with the Electrical Engineering Department, California State University at Los Angeles (UCLA), Los Angeles, CA 90095 USA. He is now with the School of Engineering, University of California, Irvine, Irvine, CA 92697-2700 USA.

Publisher Item Identifier S 0018-9480(97)01726-2.

0018–9480/97$10.00 © 1997 IEEE

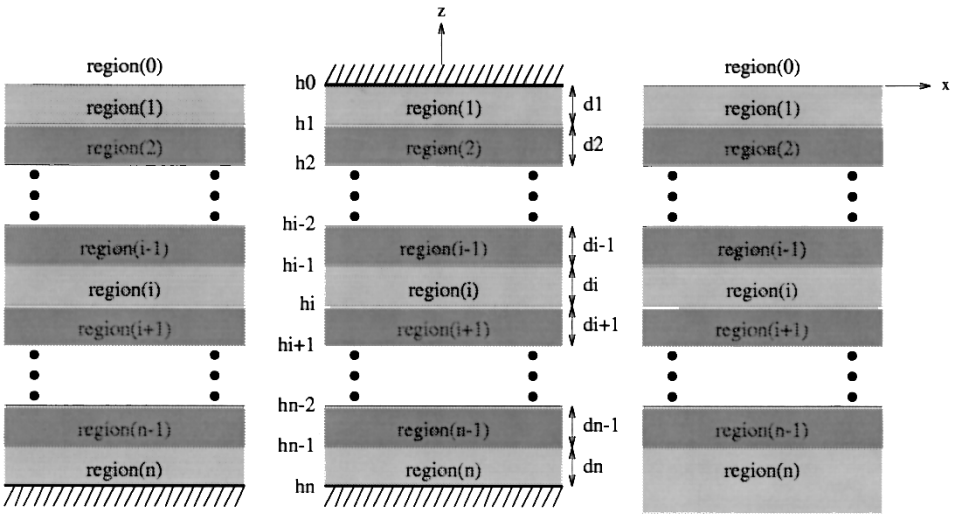

Fig. 1. Generic multilayered medium: (a) open in upper half space, (b) shielded, and (c) open in both upper and lower half spaces.

tivity and permeability ϵ_{ri} and μ_{ri}, respectively. The upper and lower ground planes are removable to represent either a shielded, semi-open, or open structure. The medium is assumed to be infinite in the x–y plane, and microstrip patterns are assumed to be of infinitesimal conductor thickness.

An EFIE can be set up, by applying the boundary condition of the zero tangential field on metal surface S, as

$$\hat{n} \times \vec{E}^{inc}(\vec{r}) = -\hat{n} \times \int_s \overline{\overline{G}}_E(\vec{r}|\vec{r}_s) \cdot \vec{J}_s(\vec{r}_s)\, dS_s \qquad \vec{r} \text{ on microstrips} \tag{1}$$

where $\overline{\overline{G}}_E$ is the dyadic electric-field Green's function, and $\vec{J}_s$ is the surface current distribution. For simplicity, the authors neglect conductor and dielectric losses. If the magnetic vector potential ($\vec{A}$) and charge scalar potential (V) as $\vec{E} = -j\omega\vec{A} - \nabla V$ are introduced, then (1) can be rewritten as an MPIE

$$\hat{n} \times \vec{E}^{inc}(\vec{r}) = \hat{n} \times [j\omega \int_s \overline{\overline{G}}_A(\vec{r}|\vec{r}_s) \cdot \vec{J}_s(\vec{r}_s)\, dS_s + \nabla \int_s G_q(\vec{r}|\vec{r}_s) q_s(\vec{r}_s)\, dS_s] \tag{2}$$

where $\overline{\overline{G}}_A$ and G_q are the dyadic Green's functions for $\vec{A}$ and V, respectively. Both Green's functions are first derived analytically in the spectral domain, then evaluated in the spatial domain using Sommerfeld integrals, discussed in the following section. $\vec{J}_s$ and q_s are the unknown distributions of the electric surface current and charge. They are connected to each other by the continuity equation. The reason the authors use the MPIE is to avoid the two-dimensional (2-D) infinite integrals with highly oscillating and slowly decaying integrands that must be evaluated in the EFIE. After removing the singular term from the MPIE's integrand, which occurs when source and field points coincide and can be computed in closed-form [17], only surface integrals with well-behaved functions over small areas need to be calculated.

A. Dyadic Green's Function

Before applying the MoM, the dyadic Green's function for a multilayered medium is derived. In [11]–[15] only the Green's function with the field point in the source layer is discussed. As a result, planar circuits in conventional microstrip with two dielectric layers can be investigated, but circuits with three or more dielectric layers cannot be dealt with. Here, the spectral-domain Green's function is derived in a general form. It can be written as the sum of TE and TM $+\hat{z}$ and $-\hat{z}$ propagating waves due to the reflection and transmission between different layers, no matter where the field point is. The generalized reflection and transmission coefficients [18] are obtained from the boundary conditions. For planar microstrip configurations, only G_A^{xx} and G_q^x due to a horizontal electric dipole (HED) are involved. They are listed as follows, depending on the location of the field point.

1) Source Layer:

$$\begin{aligned}\tilde{G}_A^{(i)xx} = {} & \frac{\mu_0\mu_{ri}}{2\gamma_i}\{e^{-\gamma_i|z-z_s|} + \tilde{M}_i^{\mathrm{TE}}[\tilde{R}_{i+}^{\mathrm{TE}} e^{-\gamma_i(2h_{i-1}-z-z_s)} \\ & + \tilde{R}_{i-}^{\mathrm{TE}} e^{-\gamma_i(z+z_s-2h_i)} \\ & + \tilde{R}_{i+}^{\mathrm{TE}}\tilde{R}_{i-}^{\mathrm{TE}}(e^{-\gamma_i(2d_i+z-z_s)} \\ & + e^{-\gamma_i(2d_i-z+z_s)})]\}\end{aligned} \tag{3}$$

$$\begin{aligned}\tilde{G}_q^{(i)x} = {} & \frac{1}{2\gamma_i\epsilon_0\epsilon_{ri}}\Big\{e^{-\gamma_i|z-z_s|} + \frac{k_i^2}{k_\rho^2}\tilde{M}_i^{\mathrm{TE}} \\ & \cdot [\tilde{R}_{i+}^{\mathrm{TE}} e^{-\gamma_i(2h_{i-1}-z-z_s)} + \tilde{R}_{i-}^{\mathrm{TE}} e^{-\gamma_i(z+z_s-2h_i)} \\ & + \tilde{R}_{i+}^{\mathrm{TE}}\tilde{R}_{i-}^{\mathrm{TE}}(e^{-\gamma_i(2d_i+z-z_s)} + e^{-\gamma_i(2d_i-z+z_s)})] \\ & - \frac{\gamma_i^2}{k_\rho^2}\tilde{M}_i^{\mathrm{TM}}[\tilde{R}_{i+}^{\mathrm{TM}} e^{-\gamma_i(2h_{i-1}-z-z_s)} \\ & + \tilde{R}_{i-}^{TM} e^{-\gamma_i(z+z_s-2h_i)} \\ & - \tilde{R}_{i+}^{\mathrm{TM}}\tilde{R}_{i-}^{\mathrm{TM}}(e^{-\gamma_i(2d_i+z-z_s)} + e^{-\gamma_i(2d_i-z+z_s)})]\Big\}.\end{aligned} \tag{4}$$

2) Outside Source Layer ($i < j$; $z > z_s$):

$$\tilde{G}_A^{(ij)xx} = \frac{\mu_0\mu_{rj}}{2\gamma_j}\overline{T}_{\rm TE}^{(ji)+}\tilde{M}_j^{\rm TE} \cdot [e^{-\gamma_j(h_{j-1}-z_s)} + \tilde{R}_{j-}^{TE}e^{-\gamma_j(z_s+h_{j-1}-2h_j)}] \cdot [e^{-\gamma_i(z-h_i)} + \tilde{R}_{i+}^{TE}e^{-\gamma_i(2h_{i-1}-h_i-z)}] \quad (5)$$

$$\tilde{G}_q^{(ij)x} = \frac{1}{2\gamma_j\epsilon_0\epsilon_{rj}k_\rho^2}\{k_j^2\overline{T}_{\rm TE}^{(ji)+}\tilde{M}_j^{\rm TE} \cdot [e^{-\gamma_j(h_{j-1}-z_s)} + \tilde{R}_{j-}^{\rm TE}e^{-\gamma_j(z_s+h_{j-1}-2h_j)}] \cdot [e^{-\gamma_i(z-h_i)} + \tilde{R}_{i+}^{\rm TE}e^{-\gamma_i(2h_{i-1}-h_i-z)}] + \gamma_j^2\overline{T}_{\rm TM}^{(ji)+}\tilde{M}_j^{\rm TM} \cdot [e^{-\gamma_j(h_{j-1}-z_s)} - \tilde{R}_{j-}^{\rm TM}e^{-\gamma_j(z_s+h_{j-1}-2h_j)}] \cdot [e^{-\gamma_i(z-h_i)} - \tilde{R}_{i+}^{\rm TM}e^{-\gamma_i(2h_{i-1}-h_i-z)}]\} \quad (6)$$

where γ_i^2 is defined as $k_\rho^2 - k_i^2$ and $k_\rho^2 = k_x^2 + k_y^2$ with k_i as the wave number of the ith layer. The HED is embedded in the jth layer, and the field point is in the ith layer. The subscripts $+$ and $-$ represent $+\hat{z}$ and $-\hat{z}$ propagating waves, respectively. The generalized reflection/transmission coefficients of TE/TM waves are denoted as $\tilde{R}^{\rm TE,\,TM}$ and $\overline{T}_{\rm TE,\,TM}$. They are defined in the Appendix. Equations (3) and (4) are the Green's functions with the field point embedded in the source layer (in this case, $i = j$). They are composed of three parts: a direct term, a single reflection, and a multiple-reflection from both upper and lower interfaces. Equations (5) and (6) are the Green's function with the field point embedded in the layer j differing from the source layer i. Because of reciprocity and the continuity of the Green's function, only the case of an HED below the field point ($i < j$) is considered here. Both $G_A^{(ij)xx}$ and $G_q^{(ij)x}$ are the multiplication of the transmission coefficient and $+\hat{z}$ propagating components at the h_i and h_{j-1} interfaces. With this spectral-domain Green's function, any configuration of planar conductors in a multilayered structure can be analyzed.

To convert the spectral-domain Green's function into the spatial domain, Sommerfeld integrals need to be evaluated. This is a very time-consuming step since the integrands are both highly oscillating and slowly decaying. Recently, several papers have suggested using complex images to approximate the remaining integral, after extracting the quasi-static and surface-wave contribution [14], [15], [19], [20]. However, the expansion terms and sampling region are strongly dependent on the layer's thickness and dielectric constant. Also, it is difficult to find the surface-wave poles for more than three layers. Therefore, in this analysis, Sommerfeld integrals, after extracting the quasi-static terms, are still evaluated by numerical integration [21]–[23]. The quasi-static terms, corresponding to the asymptotic behavior of the integrand, can be obtained by letting k_ρ approach infinity [24]. They can be transformed into analytic expressions by using the identity

$$\frac{e^{-jk_iR}}{R} = \int_0^\infty \frac{e^{-\gamma_i|z|}J_0(k_\rho\rho)k_\rho}{\gamma_i}\,dk_\rho \quad (7)$$

where $R = \sqrt{\rho^2 + z^2}$ is the observation distance. The remaining integrals, which converge very fast, are computed by Gaussian quadrature integration along a contour deformed off the real axis in the k_ρ plane, to avoid surface-wave poles. In order to accelerate the MoM computation, tables of G_A and G_q versus distance between source and field points are constructed. These tables are stored as a database and interpolated repeatedly during the MoM procedure. The same Green's function tables are valid for any new conductor shape, as long as the layer parameters remain the same.

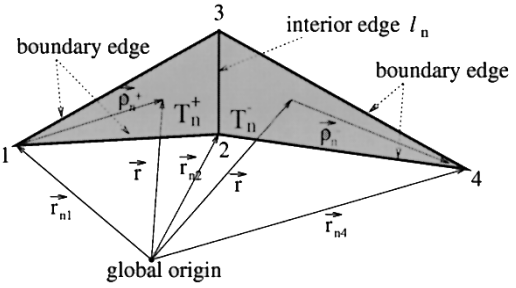

Fig. 2. Triangular-patch subdomain function.

B. The MoM's

The MoM's is applied to convert the MPIE to an algebraic linear system. The first step is to expand the unknown current distribution with a set of basis functions. To model the arbitrarily shaped microstrip geometries, the authors adopt the triangular-patch subdomain function, shown in Fig. 2, and defined as

$$\vec{tri}_n(\vec{r}) = \begin{cases} \dfrac{\ell_n}{2A_n^+}(\vec{r} - \vec{r}_{n1}) = \dfrac{\ell_n}{2A_n^+}\vec{\rho}_n^+, & \vec{r} \in T_n^+ \\ \dfrac{\ell_n}{2A_n^-}(\vec{r}_{n4} - \vec{r}) = \dfrac{\ell_n}{2A_n^-}\vec{\rho}_n^-, & \vec{r} \in T_n^- \\ 0, & \text{otherwise.} \end{cases} \quad (8)$$

This basis function can describe vector current flow. Its divergence is constant over the associated triangular face, and normal components do not exist at the exterior edges. The meshing algorithm developed in [16] is used to grid the whole circuit into small triangular facets.

The same current cell is chosen as the testing function (Galerkin's procedure) and vector identities are used to reformulate (2) as a matrix equation $[Z][I] = [V]$, containing the following matrix elements:

$$Z_{mn} = j\omega\int_{S_m}dS\int_{S_n}dS_s[\vec{tri}_m(\vec{r})\cdot\overline{\overline{G}}_A(\vec{r}|\vec{r}_s)\cdot\vec{tri}_n(\vec{r}_s)] + \frac{1}{j\omega}\int_{S_m}dS\int_{S_n}dS_s[\nabla\cdot\vec{tri}_m(\vec{r})]G_q(\vec{r}|\vec{r}_s) \cdot[\nabla_s\cdot\vec{tri}_n(\vec{r}_s)]. \quad (9)$$

In this analysis, the excitation mechanism is a series delta-gap voltage source, attached at the open end of the input line [25]. Therefore, only one nonzero element exists in the excitation vector $[V]$, and it is normalized to be 1 V. The output port(s) are open circuited.

Several numerical techniques are applied to accelerate the evaluation of matrix elements [16]. In addition to construction of Green's function tables (Section II-A), Z_{mn} is divided into nonsingular and singular parts. The singular part comes from

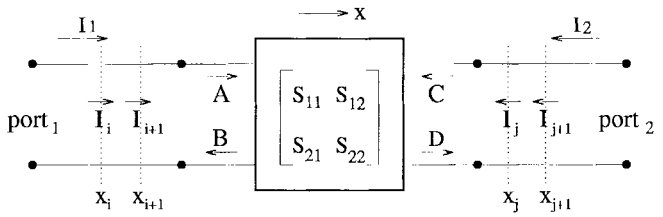

Fig. 3. A generalized two-port network.

the singularity of the spatial-domain Green's function for field points which are very close to the source point. It can be evaluated by four seven-point quadratures combined with the analytic expressions in [16] and [17]. The nonsingular part is approximated by a three-point average. The process of filling the impedance matrix is based on facets instead of interior edges to eliminate many redundant calculations [8], [16]. For example, it takes only 1 min of central processing unit (CPU) time to solve a 625-unknown problem on an IBM RS/6000 workstation.

C. Extraction of Scattering Parameters

After evaluating all elements of $[Z]$ and $[V]$, the linear system is solved for the unknown coefficients $[I]$, and scattering parameters are extracted from the current distribution. Consider the generalized two-port network in Fig. 3. I_1 and I_2 are the total current in ports 1 and 2, respectively, and can be separated into two parts: incident (A, C) and reflected (B, D) components [26]. The current distribution along the microstrip lines can be recovered from the coefficients $[I]$. At two consecutive sampling points x_i and x_{i+1} along the $port_1$ line, the currents can be expressed as

$$\begin{aligned} I_i &= I_1(x_i) \\ &= Ae^{-j\beta_p x_i} - Be^{j\beta_p x_i} \end{aligned} \tag{10}$$

$$\begin{aligned} I_{i+1} &= I_1(x_{i+1}) \\ &= Ae^{-j\beta_p x_{i+1}} - Be^{j\beta_p x_{i+1}} \end{aligned} \tag{11}$$

where β_p is the propagation constant along the microstrip line, determined in advance. Therefore, the coefficients A and B can be extracted from I_i and I_{i+1}. For the region far away from the discontinuity and the excitation point, a standing wave will be observed. Therefore, A and B are constants, independent of x. The authors can extract their values by a simple curve-fitting algorithm. C and D can be extracted from the port_2 current distribution in a similar way. To solve the scattering parameters, there are four unknowns in total, but the authors have only two equations, although more conditions should be included. The simplest way is to recalculate the current distribution with the excitation at port_2 and leave port_1 open. Following the above procedure, A^*, B^*, C^*, and D^* can be determined. Finally, the scattering parameters can be found from

$$S_{11} = \frac{BC^* - B^*C}{AC^* - A^*C} \tag{12}$$

$$S_{21} = \frac{DC^* - D^*C}{AC^* - A^*C}. \tag{13}$$

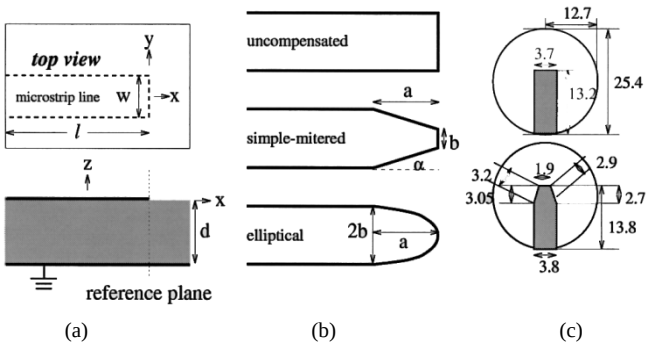

(a) (b) (c)

Fig. 4. Open-end discontinuity. (a) Rectangular open end. (b) Different open-end configurations. (c) Fabrication of open end on a quartz substrate (all in mm).

This extraction technique can be generalized easily to multiport networks, and is demonstrated to be useful and effective by the numerical examples in this paper.

III. Numerical Results and Discussion

In this section the authors present several numerical results for different configurations: regular/arbitrarily shaped, single/double-layered circuits, and antennas. The multilayered dyadic Green's function is used to solve these general geometries.

A. Microstrip Open-End Optimization

Several different calibration methods can be used to establish reference planes for measurements of microstrip circuits, some of which require an open-circuit standard. The accuracy of the measurements depends on how precisely the microstrip open is described. Also, the behavior of a true open-circuit may be more closely approximated by modifying the shape of the microstrip open. The simply mitered open end was first discussed in [27] for a coplanar waveguide (CPW) by using a stair-step approximation. The following comparison between numerical and measured results shows that the authors' analysis method provides the accuracy and flexibility needed to describe both simple (rectangular) and compensated (shaped) microstrip opens.

First the authors consider the simple microstrip open-end discontinuity [see Fig. 4(a)]. A semi-infinite microstrip line is located on the top of a single-layered substrate with $\epsilon_r = 9.9$, thickness 0.635 mm, line width 0.6 mm (for 50 Ω), and line length 12 mm. Fig. 5 compares the phase of the computed reflection coefficient to the measurement in [28]. The computed results agree with the measurement to within 1.5%. To compensate for the end effect, simply mitered as well as elliptically shaped ends were investigated [see Fig. 4(b)]. The computed performance is also shown in Fig. 5. The end effect can be compensated by choosing proper dimensions for either the mitered or elliptical end. To validate this optimization, a simply-mitered microstrip open was fabricated on a 1.5-mm quartz substrate ($\epsilon_r = 3.37$). A 0.2-μm nichrome layer was evaporated first to guarantee adhesion on the quartz, followed by a 3-μm copper layer on top [29]. The relevant dimensions of the microstrip lines are shown in Fig. 4(c). The

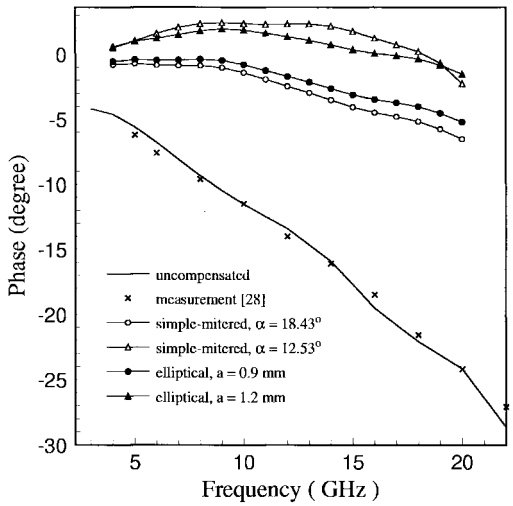

Fig. 5. The phase of reflection coefficient for different open-end configurations, $\epsilon_r = 9.9$, $d = 0.635$ mm, $w = 0.6$ mm, as in Fig. 4(a) and (b). Measurement from [28]. Simply mitered: $b = 0.23$ mm; elliptical: $2b = w$.

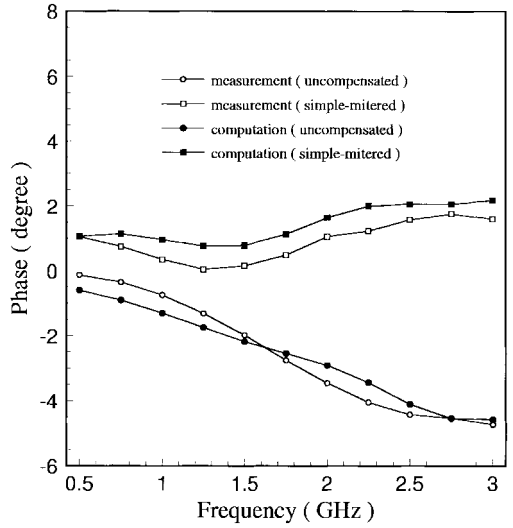

Fig. 6. The phase of reflection coefficient for uncompensated and simply-mitered open-end configurations, $\epsilon_r = 3.37$, $d = 1.5$ mm, as in Fig. 4(c).

authors chose a thick substrate with a low dielectric constant to exacerbate the end effect problem, and emphasize optimization of the geometry to minimize this phenomenon. Also, large geometries are less sensitive to fabrication tolerances. Fig. 6 shows excellent agreement between the measured and computed phase of the reflection coefficient. The simply mitered open circuit provides the best approximation to a true open circuit.

B. Microstrip Radial Stubs

The second example demonstrates the authors' ability to analyze a single-layered microstrip circuit of arbitrary shape. Fig. 7 shows a microstrip shunt-connected radial stub. The substrate has the following parameters: dielectric constant $\epsilon_r = 10.0$ and thickness $d = 0.635$ mm. The line width is 0.6 mm and is truncated (from the center) at 16.5 mm for the lower frequencies (below 8 GHz) and 7.5 mm for the

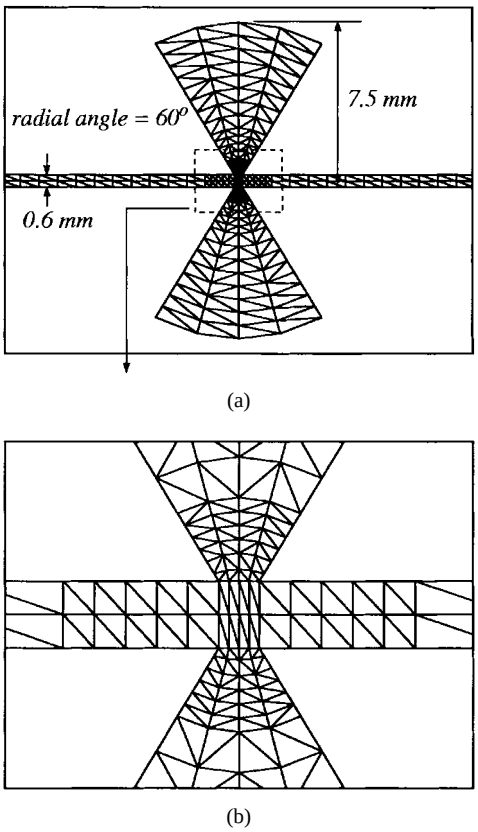

Fig. 7. Geometry and discretization of a microstrip radial stub. There is a total of 488 facets and 644 edges.

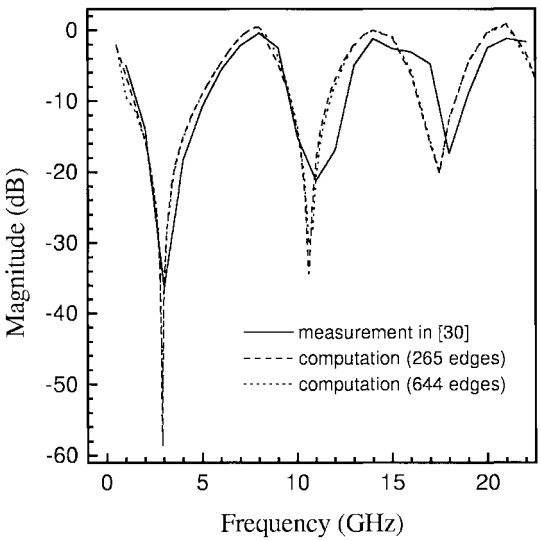

Fig. 8. Transmission coefficient of a microstrip radial stub. $\epsilon_r = 10.0$, $d = 0.635$ mm, $w = 0.6$ mm, radius = 7.5 mm, radial angle = 60°.

higher frequencies. The radius of the stub is 7.5 mm and the radial angle is 60°. To verify convergence, computations are presented for two different discretizations: the first one uses 212 triangular facets and 265 internal edges. The second one uses two cells along the transverse direction of the microstrip line and more facets along the radial direction of the stubs, making a total of 488 facets and 644 edges. The computed transmission coefficient is compared with the measurement reported in [30] and the result is shown in Fig. 8. Good

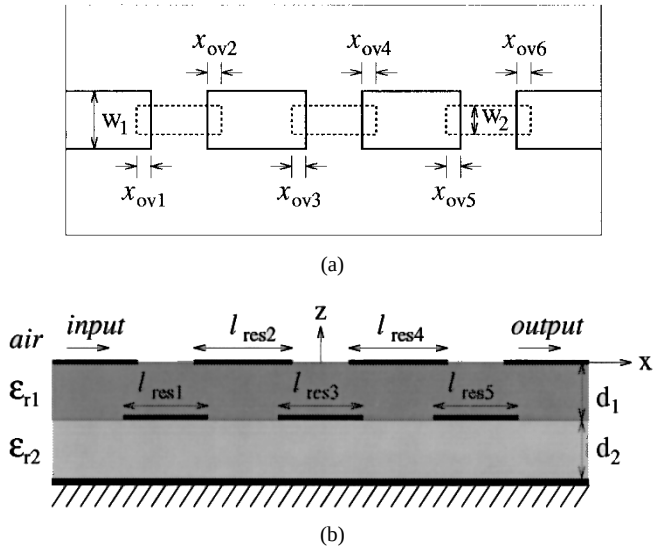

Fig. 9. Geometry of a five-section overlap-gap-coupled filter.

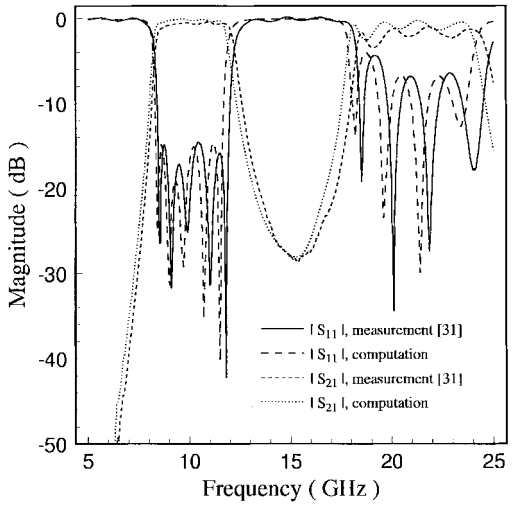

Fig. 10. Frequency response of five-section overlap-gap-coupled bandpass filter, geometry as shown in Fig. 9. ($\epsilon_{r1} = 9.8$, $\epsilon_{r2} = 2.2$, $d_1 = d_2 = 0.254$ mm, $w_1 = 0.812$ mm, $w_2 = 0.458$ mm, and Table I).

agreement and convergence over a wide frequency range have been obtained.

C. Doubled-Layered Bandpass Filter

The next example is a five-section overlap-coupled bandpass filter (see Fig. 9) [31]. It was fabricated from alumina and duroid substrates with the following tolerances: $\epsilon_{r1} = 9.8 \pm 0.2$ and $\epsilon_{r2} = 2.2 \pm 0.02$. The thicknesses d_1 and d_2 are both 0.254 mm. The line widths are $w_1 = 0.812$ mm (top) and $w_2 = 0.458$ mm (bottom). The fabricated resonator and overlap lengths are listed in Table I. Equations (5) and (6) are used here to construct the Green's function. Fig. 10 is a broad-band plot comparing the computed and measured responses. Good agreement can be seen for the low-side rejection, passband ripple, upper stopband, and second passband. However, there is a small discrepancy in center frequency. Fig. 11 (the dashed line) shows that the measured upper and lower band edges are shifted up by 220 and 130 MHz, respectively. The authors suspect two possible causes: 1) a 0.0076-mm (0.3-mL) air gap was introduced at the alumina/duroid interface by the 0.0076-mm metallization thickness of the resonators located there; and/or 2) the actual dielectric constants were below their nominal values. Therefore, the filter was analyzed again using the lower bound of the manufacturer's tolerance for each dielectric constant as well as an additional layer of air ($d_2 = 0.0076$ mm): $\epsilon_{r1} = 9.6$, $\epsilon_{r2} = 1.0$, and $\epsilon_{r3} = 2.18$. The actual alumina and duroid thicknesses were determined with a measuring microscope to be $d_1 = 0.259$ mm and $d_3 = 0.2514$ mm. These modifications produced better agreement, as seen in Fig. 11 (the dotted line).

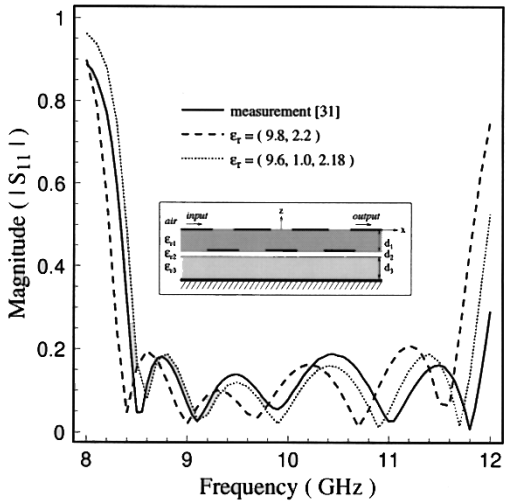

Fig. 11. Comparison of passband reflection coefficient for the modification of dielectric constant. Dashed line is from Fig. 10; Dotted line: $\epsilon_{r1} = 9.6$, $\epsilon_{r2} = 1.0$, $\epsilon_{r3} = 2.18$, $d_1 = 0.259$ mm, $d_2 = 0.0076$ mm, $d_3 = 0.2514$ mm.

TABLE I
FABRICATED RESONATOR AND OVERLAP LENGTHS OF FIVE-SECTION BANDPASS FILTER

Length (mm)	1	2	3	4	5	6
Resonator ($\ell_{\rm res}$)	6.964	6.442	7.236	6.446	6.960	—
Overlap ($x_{\rm ol}$)	1.316	0.382	0.280	0.276	0.386	1.298

D. Proximity-Coupled Circular-Patch Antenna

To illustrate the versatility of this analysis, a circular-patch antenna is considered as the final example. The configuration is shown in Fig. 12. In this example, the circular-patch antenna is fed by a proximity-coupled microstrip line, embedded in the bottom layer. The two substrate layers have the same parameters: $\epsilon_{r1} = \epsilon_{r2} = 2.62$ and $d_1 = d_2 = 1.59$ mm. Three transverse cells are used on the feed line, and 128 triangular facets compose the patch, making a total of 493 internal edges. Fig. 13 shows that the calculated input impedance agrees well with the measurement from [32]. It proves that this full-wave MPIE–MoM analysis using triangular basis functions can be applied to arbitrarily shaped multilayered microstrip antennas as well as circuits.

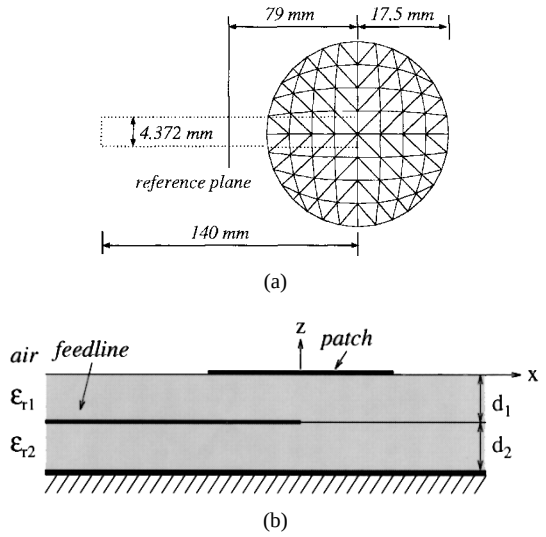

Fig. 12. Geometry of a proximity-coupled circular patch antenna. 128 facets are used to represent the patch ($\epsilon_{r1} = \epsilon_{r2} = 2.62$ and $d_1 = d_2 = 1.59$ mm).

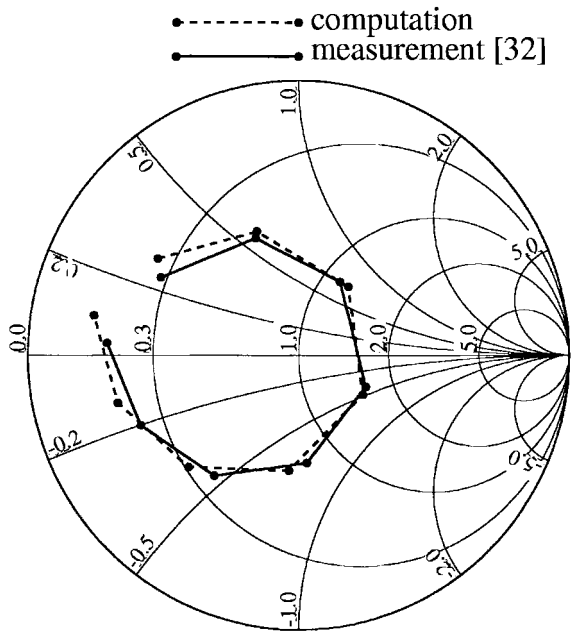

Fig. 13. The input impedance of a proximity-coupled circular patch antenna (See Fig. 12 for dimensions).

IV. Conclusion

In advanced MMIC technology, multilayered configurations have become necessary to achieve higher density. The authors have proposed this full-wave spatial-domain analysis to develop a generalized dynamic model for arbitrarily shaped circuits and antennas in a multilayered configuration. The derived dyadic Green's function can be applied to structures with any number of layers. Moreover, it is developed so that the field point and source point can be at different layers without limitation on the distance between them. In addition, triangular-patch functions allow any arbitrarily shaped planar geometry to be modeled without difficulty. Several numerical results have been presented that show excellent properties and may find promising applications in MMIC designs. This analysis provides an accurate and flexible algorithm to model microstrip antennas as well as microstrip circuits.

Appendix

The generalized reflection/transmission coefficients in (3)–(6) were introduced in [18]. They are listed here in our notation as follows:

$$\tilde{R}_{i+}^{\mathrm{TE,\,TM}} = \frac{r_{i+}^{\mathrm{TE,\,TM}} + \tilde{R}_{(i-1)+}^{\mathrm{TE,\,TM}} e^{-2\gamma_{i-1}d_{i-1}}}{1 + r_{i+}^{\mathrm{TE,\,TM}} \tilde{R}_{(i-1)+}^{\mathrm{TE,\,TM}} e^{-2\gamma_{i-1}d_{i-1}}}, \quad i = 2, 3, \cdots, n \tag{14}$$

$$\tilde{R}_{i-}^{\mathrm{TE,\,TM}} = \frac{r_{i-}^{\mathrm{TE,\,TM}} + \tilde{R}_{(i+1)-}^{\mathrm{TE,\,TM}} e^{-2\gamma_{i+1}d_{i+1}}}{1 + r_{i-}^{\mathrm{TE,\,TM}} \tilde{R}_{(i+1)-}^{\mathrm{TE,\,TM}} e^{-2\gamma_{i+1}d_{i+1}}}, \quad i = 0, 1, \cdots, n-1 \tag{15}$$

$$\tilde{M}_i^{\mathrm{TE,\,TM}} = [1 - \tilde{R}_{i+}^{\mathrm{TE,\,TM}} \tilde{R}_{i-}^{\mathrm{TE,\,TM}} e^{-2\gamma_i d_i}]^{-1} \tag{16}$$

$$\overline{T}_{\mathrm{TE,\,TM}}^{(ji)+} = \prod_{k=j}^{i+1} e^{-\gamma_k d_k} S_{k+}^{\mathrm{TE,\,TM}} \quad \text{with}\, d_j = 0 \tag{17}$$

$$S_{k+}^{\mathrm{TE,\,TM}} = \frac{1 + \mathrm{Sgn} r_{k+}^{\mathrm{TE,\,TM}}}{1 - r_{(k-1)-}^{\mathrm{TE,\,TM}} \tilde{R}_{(k-1)+}^{\mathrm{TE,\,TM}} e^{-2\gamma_{k-1}d_{k-1}}} \tag{18}$$

where *Sgn* is -1 only for the TM case of G_q^x and is 1 otherwise. The HED is embedded in the jth layer, and the field point is in the ith layer. The subscripts $+$ and $-$ represent the $+\hat{z}$ and $-\hat{z}$ propagating waves, respectively. The reflection coefficients $\tilde{R}$ can be computed by iteration, with the initial values $\tilde{R}_{1+} = r_{1+}$ and $\tilde{R}_{n-} = r_{n-}$. The parameter r is the local reflection coefficient between the adjacent layers and can be written as

$$r_{i\pm}^{\mathrm{TE}} = \begin{cases} 0, & \text{with half space} \\ -1, & \text{with ground plane} \\ \dfrac{\gamma_i \mu_{r_{i\mp1}} - \gamma_{i\mp1}\mu_{ri}}{\gamma_i \mu_{r_{i\mp1}} + \gamma_{i\mp1}\mu_{ri}} & \text{otherwise} \end{cases} \tag{19}$$

$$r_{i\pm}^{\mathrm{TM}} = \begin{cases} 0, & \text{with half space} \\ 1, & \text{with ground plane} \\ \dfrac{\gamma_i \epsilon_{r_{i\mp1}} - \gamma_{i\mp1}\epsilon_{ri}}{\gamma_i \epsilon_{r_{i\mp1}} + \gamma_{i\mp1}\epsilon_{ri}} & \text{otherwise.} \end{cases} \tag{20}$$

References

[1] P. Benedek and P. Silvester, "Equivalent capacitance of microstrip gaps and steps," *IEEE Trans. Microwave Theory Tech.*, vol. MTT-20, pp. 729–733, Nov. 1972.

[2] P. Silvester and P. Benedek, "Equivalent discontinuities capacitances for right-angle bends, T-junctions, and crossings," *IEEE Trans. Microwave Theory Tech.*, vol. MTT-21, pp. 341–346, May 1973.

[3] Y. T. Lo, D. Solomon, and W. F. Richads, "Theory and experiment on microstrip antennas," *IEEE Trans. Antennas Propagat.*, vol. AP-27, pp. 137–145, Mar. 1979.

[4] K. A. Michalski, "The mixed-potential electric field integral equation for objects in layered media," *Arch. Elek. Übertragung.*, vol. 39, pp. 317–322, Sept./Oct. 1985.

[5] J. R. Mosig, and F. E. Gardiol, "A dynamic vector potential theory for three-dimensional microstrip structures," *Mitteilungen AGEN*, no. 26, pp. 45–52, Nov. 1978.

[6] ——, "General integral equation formulation for microstrip antennas and scatterers," *Proc. Inst. Elect. Eng.*, vol. 132, pt. H, no. 7, pp. 424–432, Dec. 1985.

[7] J. R. Mosig, "Arbitrarily shaped microstrip structures and their analysis with a mixed potential integral equation," *IEEE Trans. Microwave Theory Tech.*, vol. 36, pp. 314–323, Feb. 1988.

[8] S. M. Rao, D. R. Wilton, and A. W. Glisson, "Electromagnetic scattering by surfaces of arbitrary shape," *IEEE Trans. Antennas Propagat.*, vol. AP-30, pp. 409–418, May 1982.
[9] M. J. Tsai, "Via hole modeling for multi-layered microstrip circuits," M.S. thesis, Dept. of Electrical Engineering, UCLA, Los Angeles, CA, 1993.
[10] K. A. Michalski and D. Zheng, "Electromagnetic scattering and radiation by surfaces of arbitrary shape in layered media, part II: Implementation and results for contiguous half-spaces," *IEEE Trans. Antennas Propagat.*, vol. 38, pp. 345–352, Mar. 1990.
[11] N. K. Das and D. M. Pozar, "A generalized spectral-domain Green's function for multilayer dielectric substrates with application to multilayer transmission lines," *IEEE Trans. Microwave Theory Tech.*, vol. MTT-35, pp. 326–335, Mar. 1987.
[12] J. R. James and P. S. Hall, *Handbook of Microstrip Antennas.* Stevenage, UK: Peregrinus, 1989, ch. 8, vol. 1.
[13] K. A. Michalski and D. Zheng, "Electromagnetic scattering and radiation by surfaces of arbitrary shape in layered media, part I: Theory," *IEEE Trans. Antennas Propagat.*, vol. 38, pp. 335–344, Mar. 1990.
[14] Y. L. Chow, J. J. Yang, D. G. Fang, and G. E. Howard, "Closed-form spatial Green's function for the thick substrate," *IEEE Trans. Microwave Theory Tech.*, vol. 39, pp. 588–592, Mar. 1991.
[15] M. I. Aksun and R. Mittra, "Derivation of closed-from Green's functions for a general microstrip geometry," *IEEE Trans. Microwave Theory Tech.*, vol. 40, pp. 2055–2062, Nov. 1992.
[16] W. E. McKinzie, "Electromagnetic modeling of conductor-backed aperture antennas and circuits of arbitrary shapes," Ph.D. dissertation, Dept. of Electrical Engineering, University of California, Los Angeles, CA, 1992.
[17] D. R. Wilton, S. M. Rao, A. W. Glisson, D. H. Schaubert, O. M. Al-Bundak, and C. M. Butler, "Potential integrals for uniform and linear source distribution on polygonal and polyhedral domains," *IEEE Trans. Antennas Propagat.*, vol. AP-32, pp. 276–281, Mar. 1984.
[18] W. C. Chew, *Waves and Fields in Inhomogeneous Media.* New York: Van Nostrand Reinhold, 1990, ch. 2.
[19] C. L. Chi and N. G. Alexopoulos, "Radiation by a probe through a substrate," *IEEE Trans. Antennas Propagat.*, vol. AP-34, pp. 1080–1091, Sept. 1986.
[20] ———, "An efficient numerical approach for modeling microstrip-type antennas," *IEEE Trans. Antennas Propagat.*, vol. 38, pp. 1399–1404, Sept. 1990.
[21] I. E. Rana and N. G. Alexopoulos, "Current distribution and input impedance of printed dipoles," *IEEE Trans. Antennas Propagat.*, vol. AP-29, pp. 99–105, Jan. 1981.
[22] N. G. Alexopoulos and I. E. Rana, "Mutual impedance computation between printed dipoles," *IEEE Trans. Antennas Propagat.*, vol. AP-29, pp. 106–111, Jan. 1981.
[23] P. B. Katehi and N. G. Alexopoulos, "Real axis integration of Sommerfeld integrals with applications to printed circuit antennas," *J. Math. Phys.*, vol. 24, no. 3, pp. 527–533, Mar. 1983.
[24] D. R. Jackson and N. G. Alexopoulos, "An asymptotic extraction technique for evaluating Sommerfeld-type integrals," *IEEE Trans. Antennas Propagat.* vol. AP-34, pp. 1467–1470, Dec. 1986.
[25] P. B. Katehi and N. G. Alexopoulos, "Frequency-dependent characteristics of microstrip discontinuities in millimeter-wave integrated circuits," *IEEE Trans. Microwave Theory Tech.*, vol. MTT-33, pp. 1029–1035, Oct. 1985.
[26] ———, "On the modeling of electromagnetically coupled microstrip antennas—The printed strip dipole," *IEEE Trans. Antennas Propagat.*, vol. AP-32, pp. 1179–1186, Nov. 1984.
[27] N. I. Dib and P. B. Katehi, "The effect of mitering on CPW discontinuities," in *Euro. Microwave Conf. Dig.*, Stuttgart, Germany, Sept. 9–12, 1991, pp. 223–228, 1991.
[28] G. Gronau and I. Wolff, "A simple broad-band device de-embedding method using an automatic network analyzer with time-domain option," *IEEE Trans. Microwave Theory Tech.*, vol. 37, pp. 479–483, Mar. 1989.
[29] F. De Flaviis, M. J. Tsai, S. C. Wu, and N. G. Alexopoulos, "Optimization of microstrip open end," in *IEEE AP-S Int. Symp.*, Newport Beach, CA, June 1995, vol. 3, pp. 1490–1493.
[30] F. Giannini, M. Ruggieri, and J. Vrba, "Shunt-connected microstrip radial stubs," *IEEE Trans. Microwave Theory Tech.*, vol. MTT-34, pp. 363–366, Mar. 1986.
[31] O. Fordham, M. J. Tsai, and N. G. Alexopoulos, "Electromagnetic synthesis of overlap-gap-coupled microstrip filters," in *IEEE MTT-S Int. Microwave Symp.*, Orlando, FL, May 1995, vol. 3, pp. 1199–1202.
[32] M. Davidovitz and Y. T. Lo, "Rigorous analysis of a circular patch antenna excited by a microstrip transmission line," *IEEE Trans. Antennas Propagat.*, vol. 37, pp. 949–958, Aug. 1989.
[33] T.-S. Horng, W. E. McKinzie, and N. G. Alexopoulos, "Full-wave spectral-domain analysis of compensation of microstrip discontinuities using triangular subdomain functions," *IEEE Trans. Microwave Theory Tech.*, vol. 40, pp. 2137–2147, Dec. 1992.

Ming-Ju Tsai was born in Keelung, Taiwan, on December 17, 1966. He received the B.S.E.E. degree from the National Taiwan University, Taiwan, in 1989, and the M.S.E.E. and Ph.D. degrees from the University of California, Los Angeles (UCLA), Los Angeles, CA, in 1993 and 1996, respectively.

He worked as a Research Assistant in the UCLA Electrical Engineering Department from January 1992 to June 1996. His work included numerical modeling of three-dimensional multilayered microstrip structures of arbitrary shape with applications to printed circuits and antennas. In July 1996, he joined the Wireless Components and Packaging Research Department of Lucent Technologies, Murray Hill, NJ, as a Member of the technical staff. His research interests include antenna modeling and design in wireless and personal communications systems.

Dr. Tsai is a Member of the editorial board of IEEE TRANSACTIONS ON ANTENNAS AND PROPAGATION.

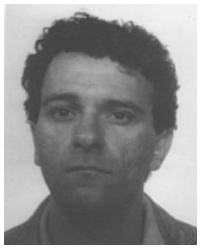

Franco De Flaviis was born in Teramo, Italy, in 1963. He received the degree in electronics engineering from the University of Ancona, Ancona, Italy, in 1990 and the M.S. degree in electrical engineering from the University of California at Los Angeles (UCLA), Los Angeles, CA, in 1994. Since 1993 he has been working toward the Ph.D. degree at UCLA.

In 1991 he worked at Telettra as a Researcher specializing in the area of microwave mixer design. In 1992 he was a Visiting Researcher at the University of California, Los Angeles (UCLA), Los Angeles, CA, working on low intermodulation mixers. His research has encompassed both theoretical and experimental studies of microwave mixers and circuits. He also synthesized low-loss ferroelectric materials for the design of microwave circuits. He is currently working in the field of numerical techniques for the analysis and design of three-dimensional microwave structures, with particular emphasis on techniques based on the time-domain approach.

Owen Fordham, photograph and biography not available at time of publication.

Nicolaos G. Alexopoulos, (S'68–M'69–SM'82–F'87) photograph and biography not available at time of publication.